The Astrophysical Journal, 713:291–303, 2010 April 10 doi:10.1088/0004-637X/713/1/291

WEAK-LENSING MASS MEASUREMENTS OF SUBSTRUCTURES IN COMA CLUSTER WITH SUBARU/SUPRIME-CAM*

N. Okabe[1,2], Y. Okura[2,3], and T. Futamase[2]
[1] Academia Sinica Institute of Astronomy and Astrophysics (ASIAA), P.O. Box 23-141, Taipei 10617, Taiwan; okabe@asiaa.sinica.edu.tw
[2] Astronomical Institute, Tohoku University, Aramaki, Aoba-ku, Sendai 980-8578, Japan
[3] National Astronomical Observatory of Japan, 2-21-1 Osawa, Mitaka, Tokyo 181-8588, Japan
Received 2008 December 12; accepted 2010 February 26; published 2010 March 19

ABSTRACT

We obtain the projected mass distributions for two Subaru/Suprime-Cam fields in the southwest region ($r \lesssim 60'$) of the Coma Cluster ($z = 0.0236$) by weak-lensing analysis and we detect eight subclump candidates. We quantify the contribution of background large-scale structure (LSS) on the projected mass distributions using Sloan Digital Sky Survey multi-bands and photometric data, under the assumption of mass-to-light ratio for field galaxies. We find that one of the eight subclump candidates, which is not associated with any member galaxies, is significantly affected by LSS lensing. The mean projected mass for the seven subclumps extracted from the main cluster potential is $\langle M_{\rm 2D}^{\rm (corr)} \rangle = (5.06 \pm 1.30) \times 10^{12}\, h^{-1}\, M_{\odot}$ after an LSS correction. A tangential distortion profile over an ensemble of subclumps is well described by a truncated singular-isothermal sphere model and a truncated Navarro–Frenk–White model. A typical truncated radius of subclumps, $r_t \simeq 35\, h^{-1}$ kpc, is derived without assuming any relations between mass and light for member galaxies. The radius coincides well with the tidal radius, $\sim 42\, h^{-1}$ kpc, of the gravitational force of the main cluster. Taking into account the incompleteness of the data area, a projection effect, and spurious lensing peaks, it is expected that the mass of the cluster substructures accounts for 19% of the virial mass, with 13% statistical error. The mass fraction of the cluster substructures is in rough agreement with numerical simulations.

Key words: galaxies: clusters: individual (Coma Cluster (A1656)) – gravitational lensing: weak – X-rays: galaxies: clusters

1. INTRODUCTION

The cold dark matter (CDM) paradigm predicts the presence of numerous substructures in dark halos on any scale, because less massive objects form earlier and become more massive through mergers. Indeed, high-resolution *N*-body simulations have shown an assembly history that subhalos continually fall into larger halos. When interior subhalos penetrate into the central region of a massive parent halo, subhalos are disrupted by its strong tidal field. As a result, the original subhalo mass is reduced by the tidal effect and becomes a part of the smoothed component of the parent halo (e.g., De Lucia et al. 2004; Gao et al. 2004). Therefore, a study of subhalo properties is of vital importance to understand the assembly history in halo environments. Furthermore, a statistical study of subhalos, such as their mass function, would offer a powerful test of the CDM model on scales less than several Mpc.

Gravitational lensing analysis on background galaxies is a unique technique to map out mass distributions of any object, such as galaxies and clusters, regardless of the dynamical state. It therefore enables us to explore substructures in primary halos and to measure directly their masses. Indeed, galaxy–galaxy lensing studies in clusters (e.g., Natarajan & Springel 2004; Natarajan et al. 2007) revealed cluster substructures and measured their mass functions under the assumption of a scaling relation between mass and light. However, a technique requiring no assumption of mass-to-light relation is of paramount importance, because subhalo size in a strong tidal field depends on its orbit parameters as well. Furthermore, we cannot rule out a possibility that gaseous galaxies in a gaseous environment of galaxy clusters are offset from subhalo centers because of ram pressure. Even a slight offset prevents us from measuring subhalo masses accurately, because the miscentering of tangential distortion profile causes a large error in mass estimations especially within inner regions (e.g., Yang et al. 2006; Johnston et al. 2007). It is therefore important to explore subhalos and measure their masses based on a weak mass reconstruction technique independent of any mass-to-light scaling relations.

As demonstrated by Okabe & Umetsu (2008), a systematic weak-lensing study on seven merging clusters in the range of $z \sim 0.055$–0.28 is capable of discovering massive substructures associated with cluster majors. However, the limit of angular resolution of reconstructed mass distributions, within the redshift range, makes it difficult to discover less massive substructures associated with cluster galaxies. On the other hand, it would be easier to detect less massive substructures in lower redshift clusters in spite of the weakness of their lensing signal, because the number of available source galaxies increases, thanks to larger apparent size of objects at lower redshift. Therefore, weak-lensing study of low-redshift clusters will provide us with a good opportunity to detect and measure smaller subhalo masses in clusters. As the first step, we select the Coma Cluster for the target to measure subhalo masses by weak-lensing analysis alone. The redshift of the Coma Cluster is 0.0236. The Coma Cluster is known as one of the most massive clusters near us. We analyze archival Subaru/Suprime-Cam data (Miyazaki et al. 2002) to measure subhalo masses found in projected mass distributions as well as cluster virial mass, and calculate the mass fraction of substructures. We also investigate lensing from background large-scale structure (LSS) in a quantitative way, using Sloan Digital Sky Survey (SDSS) multi-bands and photometric data.

The outline of this paper is as follows. We briefly describe the data analysis in Section 2 and measure the three-dimensional

* Based on data collected at the Subaru Telescope and obtained from the SMOKA, which is operated by the Astronomy Data Center, National Astronomical Observatory of Japan.

mass enclosed within a spherical region of a given radius using a tangential shear profile given in Section 3. Section 4 presents the projected distributions of mass and member galaxies, quantifies false lensing peaks, and estimates background lensing effects on the weak-lensing mass reconstruction. In Section 5, we measure the two-dimensional masses for subclumps with and without an LSS lensing correction. In Section 6, we fit a tangential shear profile over an ensemble of subclump candidates and obtain the typical truncated radius and mass of subhalos. Section 7 is devoted to the discussion. Throughout the paper, we adopt cosmology parameters $\Omega_{m0} = 0.27$ and $\Omega_\Lambda = 0.73$. At the redshift of the Coma Cluster, $1' = 20.0\,h^{-1}$ kpc.

2. DATA ANALYSIS

We retrieved two R_c image data (Yoshida et al. 2008) from the Subaru archival data (SMOKA).[4] Pointings of imaging data are the central region of $r \lesssim 30'$ from the cD galaxy NGC 4874 and the outskirts region of $r \sim 30'$–$60'$. They cover the southwest part of this cluster. The data were reduced by the same imaging process using standard pipeline reduction software for Suprime-Cam, SDFRED (Yagi et al. 2002; Ouchi et al. 2004), as described in Okabe & Umetsu (2008). Astrometry and the photometric calibration were conducted using the SDSS data catalog. The exposure times are 42 and 16 minutes for the central and outskirt regions, respectively.

Our weak-lensing analysis was done using the IMCAT package provided by N. Kaiser (Kaiser et al. 1995).[5] We use the same pipeline as Okabe et al. (2009) with some modifications followed by Erben et al. (2001; also see Okabe & Umetsu 2008). In the pipeline, we first measure the image ellipticity, e_α, from the weighted quadrupole moments of the surface brightness of each object and then correct the point-spread function (PSF) anisotropy as $e'_\alpha = e_\alpha - P_{\rm sm}^{\alpha\beta}(P_{\rm sm}*)^{-1}_{\beta\gamma}e^\gamma*$, where $P_{\alpha\beta}$ is the smear polarizability tensor and the asterisk denotes the stellar objects. We fit the stellar anisotropy kernel $(P_{\rm sm}*)^{-1}_{\alpha\beta}e^\beta*$ with the second-order bi-polynomial function in several subimages whose sizes are determined based on the typical coherent scale of the measured PSF anisotropy pattern. We finally obtain the reduced shear $g_\alpha = \gamma_\alpha/(1-\kappa) = (P_g)^{-1}_{\alpha\beta}e'_\beta$ using the pre-seeing shear polarizability tensor P_g. We adopt the scalar value $(P_g)_{\alpha\beta} = {\rm Tr}[P_g]\delta_{\alpha\beta}/2$, following the technique described in Erben et al. (2001).

We ran the pipeline for each imaging data and obtained the shear catalog of source galaxies whose magnitude ranges are 20–25 AB mag and half-light radius is $\bar{r}_h^* + \sigma(r_h^*) < r_h < 10$ pixel, where $\bar{r}_h^*$ and $\sigma(r_h^*)$ are the mean and 1σ error for stellar objects, respectively. Here, the upper limit of magnitude is determined by the outskirt data of short exposure time, although faint galaxies in the range of 25–26 AB mag are usable in the data of the central region. Since apparent sizes of unlensed galaxies, mainly cluster members, are large in general, our source galaxy selection efficiently excludes member galaxies which dilutes lensing strengths. The number density of source galaxies is $\simeq$23 arcmin^{-2}.

3. CLUSTER MASS MEASUREMENT

We measure a tangential shear component, $g_+ = -g_1\cos 2\varphi - g_2 \sin 2\varphi$, and the 45° rotated component, $g_\times = -g_1 \sin 2\varphi + g_2 \cos 2\varphi$, with respect to the cluster center, where

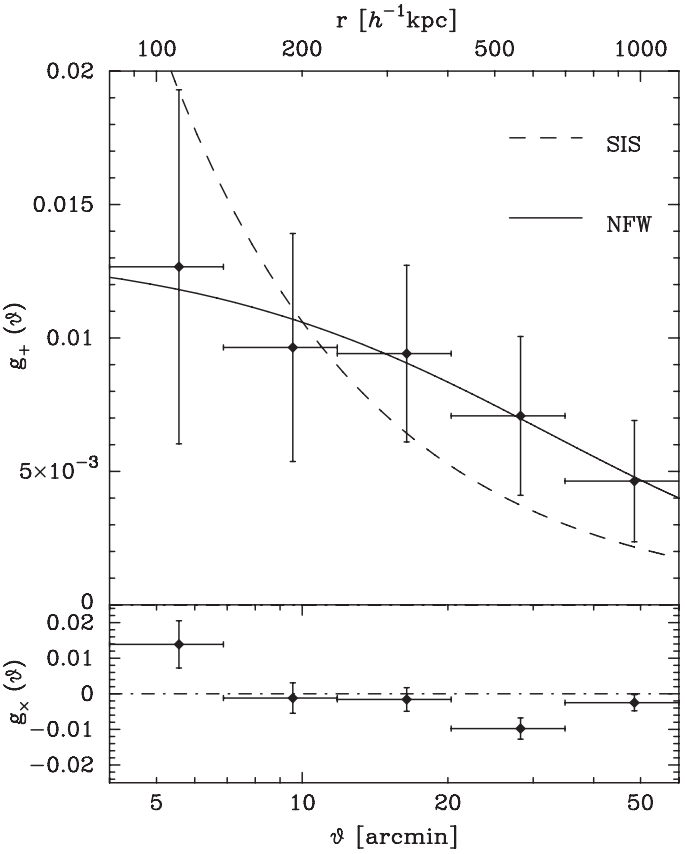

Figure 1. Profiles of tangential shear component (top panel), g_+, and the 45° rotated component (bottom panel), $g_\times$. The solid and dashed lines are the best-fit NFW and SIS models, respectively.

φ is the position angle in the counterclockwise direction from the first coordinate. Then, the profiles of shear components $g_\beta = (g_+, g_\times)$ are obtained from the weighted azimuthal average of the distortion components of source galaxies as $\langle g_\beta\rangle(\theta_n) = \sum_i u_{g,i}g_{\beta,i}/\sum_i u_{g,i}$ with a statistical weight $u_{g,i} = 1/(\sigma^2_{g,i} + \alpha^2)$, where subscripts "$n$" and "$i$" denote the nth radial bin and the ith source object, respectively. We adopt the softening constant $\alpha = 0.4$ which is a typical value of the mean rms $\bar{\sigma}_g$ over source galaxies.

There are two cD galaxies (NGC 4874 and NGC 4889) in the central region of Coma Cluster. We adopt the center of Coma Cluster as NGC 4874 because a number of luminous galaxies are concentrated around NGC 4874 in our optical image, and the peak of X-ray surface brightness is close to NGC 4874 (see also Figure 10). The shear profile covers the range of 4′–60′ with five bins. It corresponds to the first bin of Kubo et al. (2007). We fit the shear profile with the universal profile proposed by Navarro et al. (1996, hereafter Navarro–Frenk–White (NFW) profile) and a singular-isothermal sphere (SIS) halo model (see Figure 1). We assume that the redshift of source background galaxies is $\langle z_s\rangle = 1$. An uncertainty of source redshift in mass estimates is negligible because the lens distance ratio, D_{ls}/D_s, at such a low-redshift cluster weakly depends on source redshifts.

The NFW mass model is described by two parameters of the three-dimensional mass $M_{\rm NFW}(<r_\Delta)$ and the halo concentration $c_\Delta = r_\Delta/r_s$, where r_s is the scale radius and r_Δ is the radius at which the mean density is Δ times the critical mass density, $\rho_{\rm cr}(z)$, at the cluster redshift. The density profile of the NFW

[4] http://smoka.nao.ac.jp/index.jsp
[5] http://www.ifa.hawaii.edu/~kaiser/imcat/

Table 1
Best-fit Mass Models Without an LSS Lensing Correction

NFW	$\chi^2/\mathrm{dof} = 0.1/3$			
Δ	$M_{\rm NFW}(<r_\Delta)$ $(10^{14}\,h^{-1}\,M_\odot)$	c_Δ	r_Δ $(h^{-1}$ kpc)	θ_Δ (arcmin)
(1)	(2)	(3)	(4)	(5)
Vir	$8.85^{+19.87}_{-5.12}$	$3.49^{+2.55}_{-1.78}$	$1972.2^{+947.7}_{-493.7}$	$98.30^{+47.19}_{-24.54}$
200	$6.56^{+11.93}_{-3.60}$	$2.49^{+1.93}_{-1.34}$	$1403.7^{+579.2}_{-326.8}$	$70.15^{+28.94}_{-16.33}$
500	$4.05^{+5.01}_{-2.00}$	$1.53^{+1.34}_{-0.90}$	$880.7^{+270.5}_{-177.6}$	$44.01^{+13.52}_{-8.87}$
2500	$1.18^{+0.57}_{-0.42}$	$0.61^{+0.67}_{-0.40}$	$341.2^{+47.5}_{-46.3}$	$17.05^{+2.38}_{-2.31}$
SIS	$\chi^2/\mathrm{dof} = 4.4/4$			
σ_v (km s^{-1}) (6)				
$671.1^{+73.4}_{-69.5}$				

Notes. Column 1: over-densities $\Delta = \Delta_{\rm vir}$, 200, 500, and 2500. Column 2: best-fit three-dimensional cluster mass for the NFW mass model within r_Δ at which the mean interior density is Δ times the critical mass density, $\rho_{\rm cr}(z)$, at the cluster redshift (Equation (2)). Column 3: best-fit concentration parameter c_Δ. Column 4: radius r_Δ corresponding to the mass $M_{\rm NFW}(<r_\Delta)$. Column 5: angular size of radius r_Δ Column 6: best-fit velocity dispersion for the SIS model (Equation (4)). The χ^2/dof is the chi-square for best fits and the degree of freedom.

mass model is expressed in the form of

$$\rho_{\rm NFW}(r) = \frac{\rho_s}{(r/r_s)(1+r/r_s)^2}. \quad (1)$$

The three-dimensional cluster mass for the NFW mass model is obtained by

$$M_{\rm NFW}(<r_\Delta) = \frac{4\pi\rho_s r_\Delta^3}{c_\Delta^3} m(c_\Delta), \quad (2)$$

with

$$m(x) = \log(1+x) - \frac{x}{1+x}. \quad (3)$$

For reference with other works, results of mass and concentration parameter within radii for $\Delta = 2500$, 500, and 200 and virial overdensity $\Delta = \Delta_{\rm vir} \simeq 98$ (Nakamura & Suto 1997) are listed in Table 1. The density profile of the SIS mass model is given by

$$\rho_{\rm SIS}(r) = \frac{\sigma_v^2}{2\pi G r^2}, \quad (4)$$

where the one-dimensional velocity dispersion, σ_v^2, is a parameter.

The resulting parameters are summarized in Table 1. Since the covering area of the data is small, $\lesssim 60'$, the NFW mass is not constrained well. This is why the mass M_Δ determined by fitting the tangential shear is sensitive to the tangential distortion at r_Δ (Okabe et al. 2009). Since the best-fit virial radius is $\sim 98.'5$, we require data of a wider region to measure the cluster mass accurately. We note that the χ^2 is quite small because the number of background galaxies is scarce and the intrinsic ellipticity noise is large. The covering area of our data is only $\sim$16% within $60'$. If the data cover the whole area, the error would improve $\sim$2.5 times and the χ^2 would become close to 1.

Table 2
Best-fit Mass Models with an LSS Lensing Correction (see Sections 3 and 4.4)

NFW	$\chi^2/\mathrm{dof} = 0.1/3$			
Δ	$M_{\rm NFW}(<r_\Delta)$ $(10^{14}\,h^{-1}\,M_\odot)$	c_Δ	r_Δ $(h^{-1}$ kpc)	θ_Δ (arcmin)
(1)	(2)	(3)	(4)	(5)
Vir	$8.92^{+20.05}_{-5.17}$	$3.50^{+2.56}_{-1.79}$	$1972.2^{+947.7}_{-493.7}$	$98.56^{+47.36}_{-24.67}$
200	$6.61^{+12.06}_{-3.63}$	$2.50^{+1.94}_{-1.34}$	$1407.7^{+581.6}_{-328.4}$	$70.35^{+29.07}_{-16.41}$
500	$4.09^{+5.07}_{-2.01}$	$1.57^{+1.34}_{-0.90}$	$883.4^{+272.0}_{-178.0}$	$44.15^{+13.59}_{-8.90}$
2500	$1.19^{+0.58}_{-0.42}$	$0.61^{+0.67}_{-0.40}$	$342.5^{+47.7}_{-45.0}$	$17.11^{+2.38}_{-2.25}$
SIS	$\chi^2/\mathrm{dof} = 4.4/4$			
σ_v (km s^{-1}) (6)				
$673.0^{+73.7}_{-69.7}$				

Note. See the caption of Table 1.

The NFW virial mass changes -0.5% and +0.8% if the mean source redshift is changed to $\langle z_s\rangle = 1.2$ and 0.8, respectively.

We also perform a fitting taking into account an LSS lensing effect. The estimation of the LSS effect on the lensing signal will be described in detail in Section 4.4. The best-fit parameters are summarized in Table 2. The LSS effect is not significant on cluster mass estimate.

4. PROJECTED DISTRIBUTIONS OF MASS AND GALAXIES

4.1. Mass, Number Density, and Luminosity Maps

We reconstruct the lensing convergence field, κ, from the shear field, using the Kaiser & Squires (1993) inversion method, following Okabe & Umetsu (2008). In map making, we pixelize the shear data into a pixel grid using a Gaussian smoothing kernel $w_g(\theta) \propto \exp[-\theta^2/\theta_g^2]$ and a statistical weight $u_{g,i}$ (Section 3). The shear field at a given position ($\boldsymbol{\theta}$) is obtained by $\bar\gamma_\alpha(\boldsymbol{\theta}) = \sum_i w_g(\boldsymbol{\theta}-\boldsymbol{\theta}_i)u_{g,i}\gamma_{\alpha,i}/\sum_i w_g(\boldsymbol{\theta}-\boldsymbol{\theta}_i)u_{g,i}$, where the weak limit $g_\alpha \approx \gamma_\alpha$ is assumed. We employ the smoothing FWHM $= \sqrt{4\ln 2}\theta_g = 2.'00$. The error variance for the smoothed shear is given as $\sigma_{\bar g}^2(\boldsymbol{\theta}) = (\sum_i w_g(\boldsymbol{\theta}-\boldsymbol{\theta}_i)^2 u_{g,i}^2\sigma_{g,i}^2)/(\sum_i w_g(\boldsymbol{\theta}-\boldsymbol{\theta}_i)u_{g,i})^2$. We have used $\langle g_{\alpha,i}\, g_{\beta,j}\rangle = (1/2)\sigma_{g,i}^2\delta^{\rm K}_{\alpha\beta}\delta^{\rm K}_{ij}$, with $\delta^{\rm K}_{\alpha\beta}$ and $\delta^{\rm K}_{ij}$ being Kronecker's delta. In the linear map-making process, the pixelized shear field is weighted by the inverse of the variance.

The resulting E-mode and B-mode maps of lensing fields are shown in panels (b) and (c) of Figures 2 and 3 which cover the central region ($26' \times 26'$) and the outskirts ($21' \times 21'$), respectively. Contours are spaced in a unit of 1σ reconstructed errors. As seen in panels (a) and (b), we find eight candidates of mass clumps whose significance is over 3σ level. Panel (a) in Figures 2 and 3 shows the Subaru R_c-band images overlaid with contours of reconstructed mass distributions. We labeled subclumps as shown in panel (a). The significance levels of mass clumps are lower than those of other clusters at the redshift range $z \sim 0.055$–0.28 (Okabe & Umetsu 2008). The B-mode map (panel (c)) in the central region shows two clumps over 3σ close to clump candidates 4 and 2 (3.5σ and 3.9σ).

We retrieve the SDSS DR7 catalog (Abazajian et al. 2009) from the SDSS CasJobs Web site[6] in order to investigate

[6] http://casjobs.sdss.org/

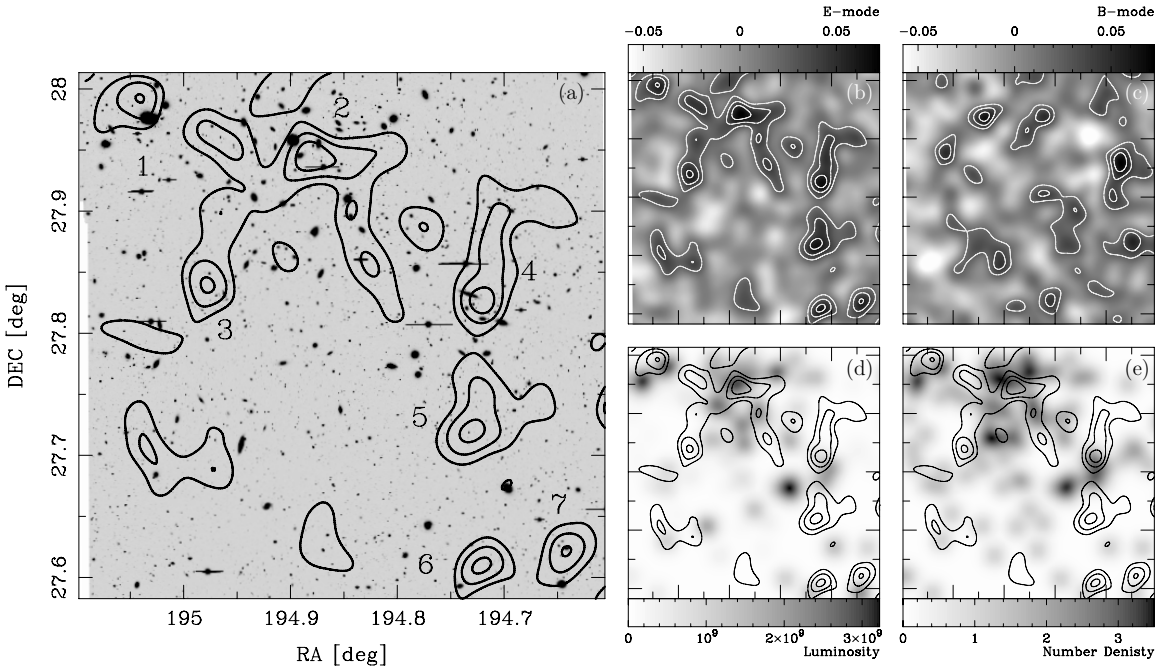

Figure 2. Panel (a) shows the Subaru R_c-band image of the central $26' \times 26'$ cluster region. Two cD galaxies (NGC 4874 and NGC 4889) are located around the northeast boundary. Overlaid are contours of the reconstructed projected mass distribution, spaced in a unit of 1σ reconstruction error ($\delta\kappa = 0.018$). The Gaussian FWHM is $2'.00$. The identified subclumps are labeled in panel (a). Panels (b) and (c) show the lensing κ (E-mode) and B-mode fields. Panels (d) and (e) show the cluster luminosity and density distributions in the SDSS i' band smoothed to the same angular resolution of the mass map, respectively. Seven clump candidates are found in the central region.

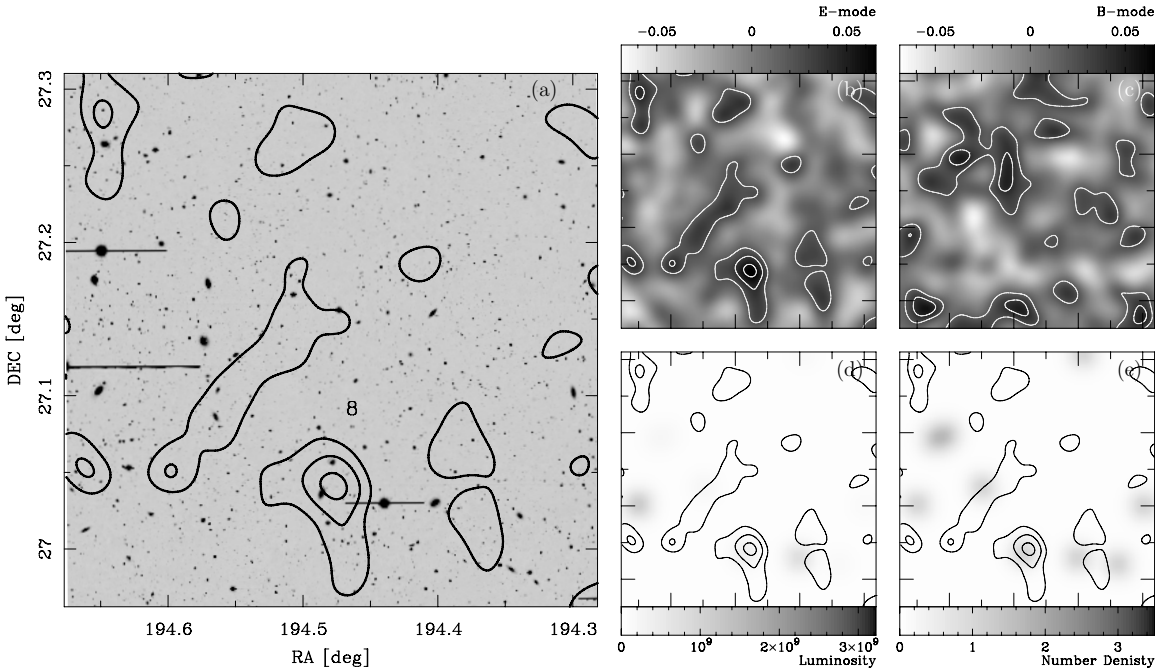

Figure 3. Panel (a) shows the Subaru R_c-band image of the outskirts $21' \times 21'$ cluster region. Overlaid are contours of the reconstructed projected mass distribution, spaced in a unit of 1σ reconstruction error ($\delta\kappa = 0.020$). The Gaussian FWHM is $2'.00$. The identified subclumps are labeled in panel (a). Panels (b) and (c) show the lensing κ (E-mode) and B-mode fields. The clump 8 is far $\sim 58'$ from cD galaxy NGC 4874. Panels (d) and (e) show the cluster luminosity and density distributions in the SDSS i' band smoothed to the same angular resolution of the mass map, respectively. One clump candidate is found in the outskirts.

member galaxy distributions. We select bright member galaxies by criteria of $i' < 19$ AB mag and $|(g'-i')-(-0.05i'+2.04)| < 0.14$, where we use *psfMag* for magnitude and *modelcolor* for color. We convert from apparent to absolute magnitudes by using the k-correction for early-type galaxies under the assumption that all member galaxies are located at a single cluster redshift. The galaxy luminosity and density projected distributions are obtained using the same kernel of weak-lensing mass reconstruction. The overall mass distribution appears to be similar to the galaxy luminosity and density distributions. In particular, six out of the eight mass candidates, except for clumps 3 and 5, host bright galaxies. At clump candidate 3, groups of faint member galaxies were known (Conselice & Gallagher 1999), while no galaxy group is found at the candidate 5 region.

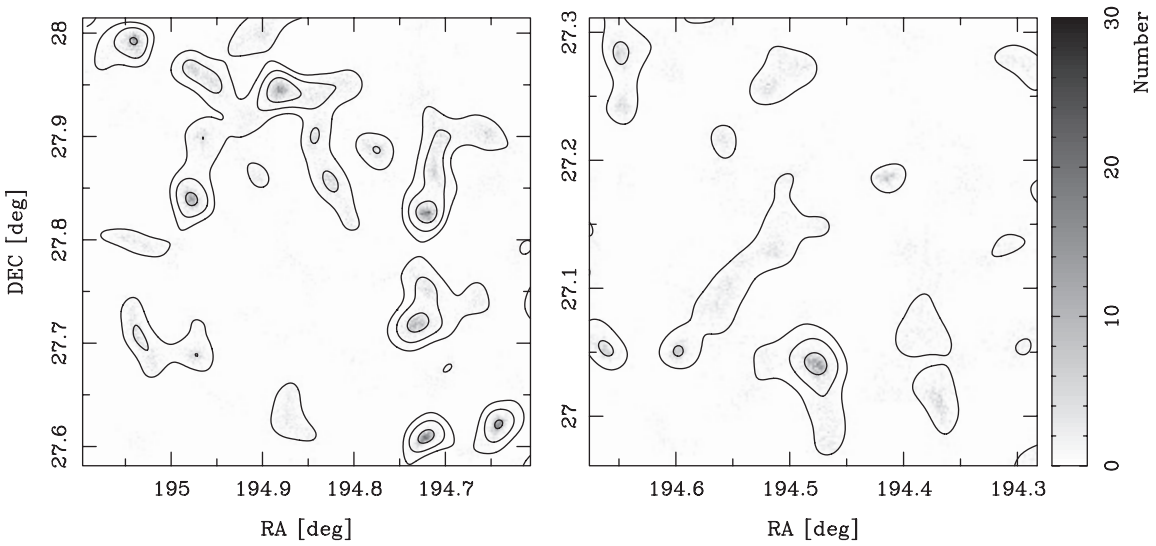

Figure 4. Histogram maps of centroid of mass peaks, whose significance level is above 3σ, that appeared in 1000 bootstrap re-sampling mass reconstructions. Contours are the same as in Figures 2 and 3. Left and right panels are the central and outskirts regions, respectively.

Table 3
Projected Mass for Subclump Candidates

ID	S/N	ν	$P_{\rm spur}$ %	$b_{\rm map}$	$M_{\rm 2D}$ ($10^{12}\,h^{-1}\,M_\odot$)	$M_{\rm 2D}^{\rm (corr)}$ ($10^{12}\,h^{-1}\,M_\odot$)	(R.A., Decl.) (deg)	Name	$d_{\rm off}$ (arcmin)
(1)	(2)	(3)	(4)	(5)	(6)	(7)	(8)	(9)	(10)
1	3.1	3.6	0.0	0.0	8.01 ± 1.05	7.70 ± 1.05	(195.042, 27.996)	NGC 4889	1.2
2	3.9	3.7	...	...	4.28 ± 0.83	4.56 ± 0.83	(194.882, 27.948)	NGC 4874	1.2
3	3.2	2.9	0.4	1.3	5.03 ± 0.87	5.29 ± 0.87	(194.980, 27.843)	SA 1656-054	1.2
4	3.6	3.2	0.0	0.0	3.49 ± 0.74	3.73 ± 0.74	(194.722, 27.829)	SDSS J125848.72+274837.5	0.7
5	3.4	3.1	12.2	41.1	5.95 ± 1.08	2.74 ± 1.08	(194.732, 27.722)	...	...
6	3.3	3.1	0.3	1.0	4.63 ± 0.84	4.54 ± 0.84	(194.724, 27.612)	SDSS J125858.10+273540.9	1.4
7	3.1	3.1	0.1	0.3	6.07 ± 1.24	7.32 ± 1.24	(194.643, 27.625)	NGC 4853	1.7
8	3.3	3.4	1.8	8.2	5.90 ± 1.32	4.61 ± 1.32	(194.475, 27.044)	SDSS J125756.65+270215.0	0.8

Notes. Column 1: name of subclump candidate. Column 2: S/N in mass maps. Column 3: $\nu = \kappa/\kappa_{\rm rms}$. The rms $\kappa_{\rm rms}$ is obtained by 1000 Monte Carlo simulations. Column 4: probability of the spurious lensing peak considering contributions of the main cluster, LSS effect, and intrinsic noises. Column 5: bias by the LSS effect and intrinsic noise for a preference to detect a clump in the convergence field of the main cluster, defined as $b_{\rm map} = P_{\rm spur}^{\rm (LSS)}/\langle P_{\rm spur}^{\rm (noise)}\rangle$. Column 6: projected mass for subclump without considering background LSS lensing effects. Column 7: projected mass for the subclump with a correction of LSS lensing effects. Column 8: central positions for mass measurements. Column 9: name of galaxies in the mass clump candidate. Column 10: angular distance, $d_{\rm off}$, between luminous galaxy in the clump candidate and centroid position for mass measurements. We note that they are consistent with galaxy positions within the uncertainty of centroid position for clump candidates (FWHM $\simeq 2'$).

We list the luminous galaxy associated with each candidate in Table 3. We do not always detect mass structures for all known groups or luminous galaxies. There are three possibilities for this. First, the LSS lensing effect prevents us from detecting lensing signals. Second, dark matter halos associated with member galaxies are less massive than the detection limit (3σ), $3 \times (\pi\theta_g^2 \Sigma_{\rm cr}\delta\kappa) \sim 3 \times 10^{12}\,h^{-1}\,M_\odot$. Third, dark halos lose their mass by the tidal force of the main cluster and then are smoothly distributed within the smoothing scale of mass reconstruction.

4.2. Bootstrap Re-sampling Mass Reconstructions

We run 1000 bootstrap simulations for mass reconstruction in order to investigate the realization of mass clumps. In each reconstruction, we generate a bootstrap data set by randomly choosing galaxies, with replacement, from the original shear catalog and then identifying mass clumps whose significance level is more than 3σ. Figure 4 shows the resulting distributions of the histogram of the appearance of mass peaks. These distributions are well associated with mass clumps. The radii at which 68% of the centroid positions contain are 0.′8–3.′0. Therefore, the detected lensing peaks are realized well in the shear catalog.

4.3. Monte Carlo Realizations

We next construct a noise map, $\kappa_{\rm rms}$, from 1000 Monte Carlo realizations, following Miyazaki et al. (2007). The position and shear components of the background galaxy catalog are randomly shuffled in each realization. A mass map for a new background catalog is reconstructed by applying the same procedure as making the original κ maps. We estimate the rms noise in each pixel and make the noise maps, $\kappa_{\rm rms}$, for the central region and the outskirts. Noise maps are not changed even if we randomly choose half of the catalog. The significance maps, $\nu = \kappa/\kappa_{\rm rms}$, are obtained by dividing the original κ maps by the $\kappa_{\rm rms}$ map. The resulting ν and $\kappa_{\rm rms}$ maps for both E- and B-modes are shown in Figure 5. The variation along the left and top edges of the $\kappa_{\rm rms}$ map in the central region is smaller than in the other region. This is why fewer galaxies exist around the boundary of the optical image. The significance maps, ν, are consistent with the original E- and B-mode maps. The significance for subclump

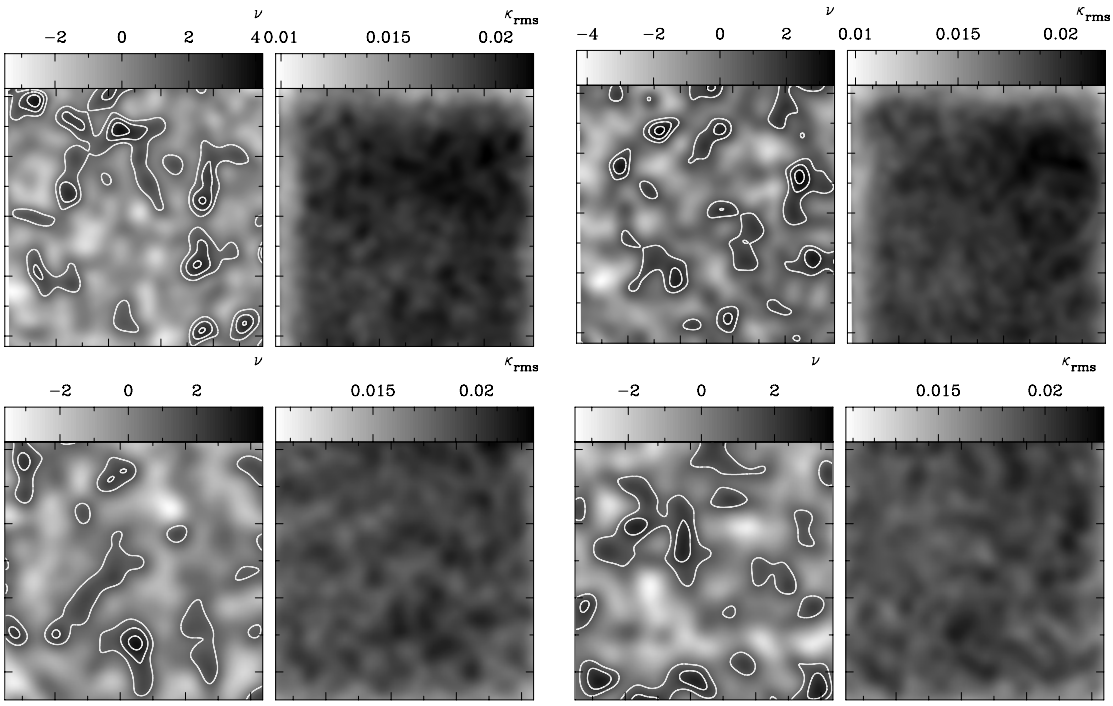

Figure 5. Top left: maps for significance $\nu = \kappa/\kappa_{\rm rms}$ (left) and noise $\kappa_{\rm rms}$ (right) for E-mode in the central region, based on 1000 Monte Carlo realizations. The contours are spaced by $\nu = 1$, 2, and 3. Top right: same maps for B-mode in the central region as the top-left panel. Bottom left: same maps for E-mode in the outskirts. Bottom right: the same maps for B-mode in the outskirts.

candidates, ν, is also consistent with the original signal-to-noise ratio (S/N; Table 3).

Are the positions of E-mode and B-mode peaks correlated? In the central region, two B-mode peaks with significance level above 3σ appear close to E-mode peaks. We calculate the probability, $P_{\rm EB}$, as a function of the distance between E- and B-mode peaks that appear in Monte Carlo realizations. The following result does not change even when we use only half of the realization data. Since the appearance probability is proportional to the area size, we also compute the probability, $P_{\rm rnd}$, that E- and B-mode peaks are randomly and independently located in each pixel. Figure 6 shows the appearance probabilities, $P_{\rm EB}$, for the central region and the outskirts, which roughly agree with the probability of the white-noise case. A slight excess of the ratio $P_{\rm EB}/P_{\rm rnd}$ is found in the range of $\theta < 10'$, but the probability is quite small. Since they are not significant, we cannot identify fake E-mode peaks using the distance from B-mode peaks. The probabilities of large distance $>20'$ are smaller than unity, because few peaks appear around the edge. Indeed, the appearance probability in 1 pixel within $2'$ width from the boundary is about one-thirds of that in the rest region. The probability of spurious lensing peaks will be evaluated considering the LSS lensing effect (Section 4.5).

4.4. Projection Effects

Since Coma Cluster is quite close to us, we cannot rule out a possibility that lensing signals by background structures significantly contribute to the observed ones. In this subsection, we quantify the projection effect by background structures on local convergence peaks appeared in the mass maps, based on the observational data, rather than a theory. In this paper, we use the shear catalog derived from one passband data alone, which makes it quite difficult to measure the contributions of background structures on lensing signals.

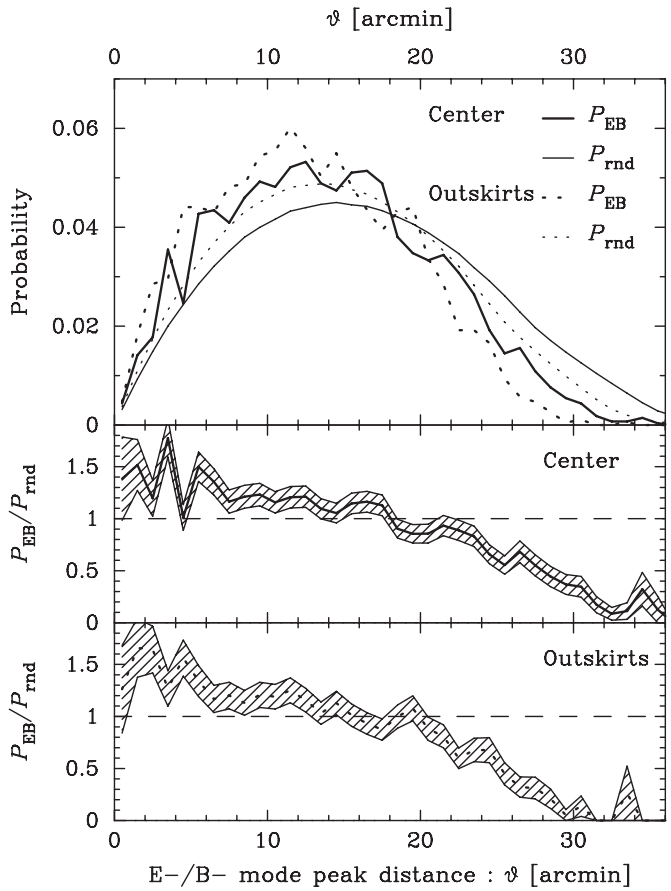

Figure 6. Top: appearance probabilities as a function of distance between E- and B-mode peaks for the central region and the outskirts. $P_{\rm EB}$ is the appearance probability obtained by 1000 Monte Carlo realizations. $P_{\rm rnd}$ is the probability that E- and B-mode peaks are randomly and independently appeared. Middle: ratio of $P_{\rm EB}/P_{\rm rnd}$ for the central region. Bottom: ratio of $P_{\rm EB}/P_{\rm rnd}$ for the outskirts.

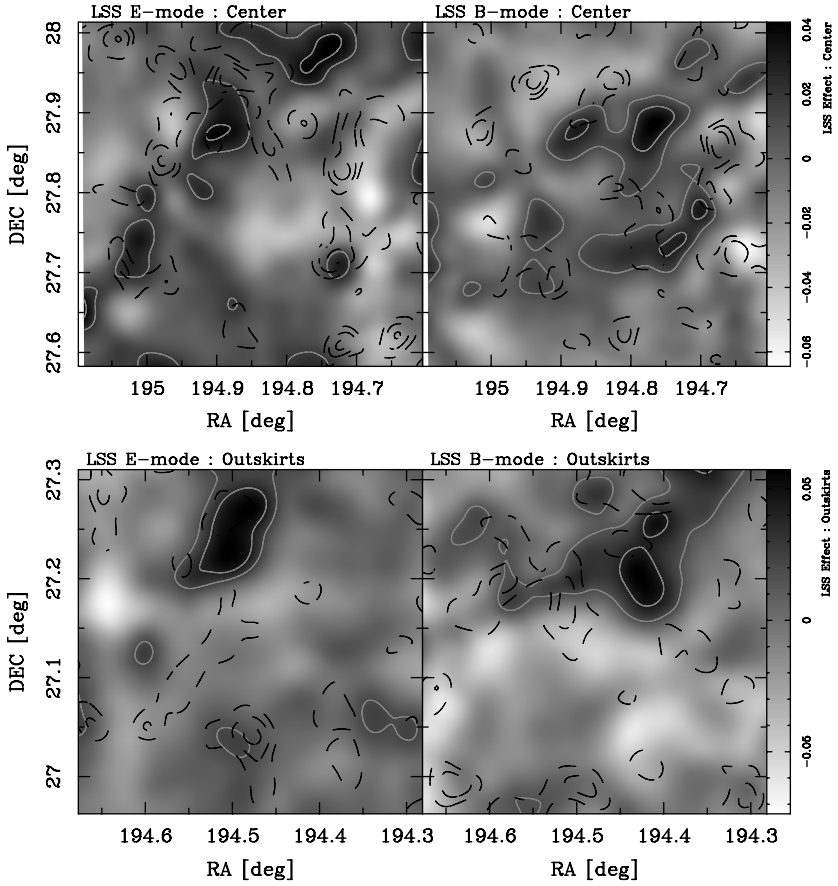

Figure 7. *E*- and *B*-mode maps reconstructed by the background LSS model alone. Top left: *E*-mode map in the central region. Top right: *B*-mode map in the central region. Bottom left: *E*-mode map in the outskirts. Bottom right: *B*-mode map in outskirts. The box sizes and contour scales are the same as those in Figures 2 and 3. Gray solid and black dashed lines show contours derived from LSS and observed shears, respectively. There are three LSS structures with a size of a few arcminutes at a $\sim 2\sigma$ level. In particular, the LSS convergences at a $\sim 1\sigma$ level are found in the clump candidates 5 and 8.

The SDSS DR7 data (Abazajian et al. 2009), on the other hand, allow us to quantify the contribution, because huge multi-band data with photometric redshifts are available. We retrieved the data in the region of $10^\circ \times 10^\circ$ ($190^\circ \leqslant$ R.A. $\leqslant 200^\circ$ and $23^\circ \leqslant$ decl. $\leqslant 33^\circ$). Since there is no candidate for galaxy clusters or groups at higher redshift in the Subaru data field by visual checks, at least, we expect to ignore contributions of background clusters/groups in our data field. We quantify the projection effect by field galaxies with photometric catalog under the assumption of mass-to-light scaling relations (Guzik & Seljak 2002). First, we select galaxy catalog by $r' < 21$ and $z_{\rm ph} - z_l > \delta z = \sigma_{v,\rm max}(1 + z_l)/c \simeq 0.01$, taking into account the uncertainty of the photometric redshift due to line-of-sight velocities of member galaxies. Here, $z_{\rm ph}$ is the photometric redshift of each galaxy, c is the light velocity, and $\sigma_{v,\rm max} = 3000$ is the maximum of the line-of-sight velocity (Rines et al. 2003). The following results do not change even when we choose the redshift ranges of $0.5\delta z$ and $2\delta z$, because a relative contribution of low-redshift galaxies in the lensing signal is quite small. The resulting galaxy catalog has a peak at $z_{\rm ph} \sim 0.5$–0.6 in the histogram of photometric redshifts for faint galaxies ($20 < r' < 21$) in DR6 data (Oyaizu et al. 2008). If the spectroscopic data of a galaxy are available, we utilize a spectroscopic redshift instead of photometric one. Next, we calculate the multi-band luminosities ($u'g'r'i'z'$) within a radius of $1.^\circ 93$ from each position of galaxy in the faint shear catalog, corresponding to 30 Mpc at $z = 0.5$ in order to consider contributions from unknown clusters/groups around $z = 0.5$, because the two-halo term in the tangential shear measurements (Seljak 2000; Mandelbaum et al. 2005) dominates around a few tens of Mpc (Johnston et al. 2007). Third, we calculate individual galaxy masses from the multi-band luminosities ($u'g'r'i'z'$) assuming the mass-to-light ratios obtained by SDSS bands (Guzik & Seljak 2002). The assumed mass-to-light ratio is in agreement with the results of other bands (Hoekstra et al. 2005). Since we adopt the mass and luminosity scaling relation for a galaxy, the mass of an overdensity region at which a distribution of galaxies is concentrated might be overestimated. Finally, we assume the mass–concentration relation (Duffy et al. 2008) to estimate NFW shear signals at each galaxy position in the background shear catalog and add them all. The luminosity scaling relations in multi-bands are complementary to each other in calibrating the lensing signals from background LSSs. If the assumed mass–luminosity relation is adequate, the reduced shears, g_α, estimated in each band should coincide with those in other bands. The resulting shears in the $u'g'i'$ bands are systematically inconsistent with all other bands, while the shears in the $r'z'$ bands have a tight correlation. We hereafter adopt $g_\alpha^{(\rm LSS)} = (g_\alpha^{(r')} + g_\alpha^{(z')})/2$ as a model of lensing signals from background LSSs.

We reconstruct the lensing convergence fields with the same kernel of mass maps (Section 4.1) using LSS contributed shears alone. Here, we do not add intrinsic shape noises for galaxies as well as shears from the main cluster, in order to investigate

the LSS lensing effect only. Figure 7 shows the resulting E- and B-mode maps. The S/N for the background LSS convergence field is at the $\sim 2\sigma$ level. In subclump candidates 5 and 8, peaks of $\sim 1\sigma$ are found in the LSS field, while no galaxy concentration in the SDSS catalog is found there. It indicates a possibility that an appearance of two clumps in the mass maps is biased by an LSS lensing effect.

4.5. Probability of Spurious Lensing Peaks

We next investigate the probability of detecting spurious lensing peaks by a composition of the LSS and main cluster lensing signals, and intrinsic shapes. We consider shears composed of $g_\alpha = g_\alpha^{(\rm main)} + g_\alpha^{(\rm LSS)} + e_\alpha^{(\rm int)}$, where $g_\alpha^{(\rm main)}$ is a best-fit NFW model in Section 3 and $e_\alpha^{(\rm int)}$ is an intrinsic shape. We produce the intrinsic ellipticities with a Gaussian distribution whose mean value is $|e_\alpha^{(\rm int)}| = 0$ and the standard deviation is $|\delta e_\alpha^{(\rm int)}| = 0.28$, corresponding to observed shear distributions. We then reconstruct mass maps and identify the mass peaks above the 3σ level, using the same procedures in Section 4.1. We repeat this 1000 times. The probability, $P_{\rm spur}^{(\rm LSS)}$, of detecting spurious lensing peak within a smoothing scale of each mass clump candidate, except for the main cluster center, is summarized in Table 3. The probabilities for clump candidates 5 and 8 are $P_{\rm spur,5}^{(\rm LSS)} = 12.2\%$ and $P_{\rm spur,8}^{(\rm LSS)} = 1.8\%$, respectively. They are much higher than those for the other clump candidates, $P_{\rm spur}^{(\rm LSS)} < 0.4\%$. We perform the same steps without LSS lensing signals ($g_\alpha = g_\alpha^{(\rm main)} + e_\alpha^{(\rm int)}$). The probabilities for candidates 5 and 8 are $P_{\rm spur,5}^{(\rm noise)} = 0.7\%$ and $P_{\rm spur,8}^{(\rm noise)} = 0.9\%$, respectively. The probability of counting spurious peaks in the candidate 5 region becomes significantly higher due to the LSS lensing effect. We also compute the averaged probability in the region excluding clump candidates in the Monte Carlo simulation taking into account the main cluster and intrinsic noises. The resulting averaged probabilities are $\langle P_{\rm spur}^{(\rm noise)}\rangle = 0.30\%$ and 0.22% in the central and outer regions, respectively. Here, we assume that the realization for spurious peaks is Poissonian. The probabilities for candidate 5 and 8 regions are still higher even without LSS effects. It might be due to distributions for sheared galaxies. We define the *bias* for a preference to detect a clump in weak mass reconstruction as $b_{\rm map} = P_{\rm spur}^{(\rm LSS)}/\langle P_{\rm spur}^{(\rm noise)}\rangle$. As summarized in Table 3, the biases for candidates 5 and 8 are significantly higher than those for other candidates. The appearances for candidates 5 and 8 in the reconstructed mass maps are likely to be due to background LSS lensing distortions, at least partially. In the following two sections, we will quantify this more accurately based on two complementary mass measurements using shears, because each pixel in the convergence field is correlated by a smoothing kernel.

5. PROJECTED MASS MEASUREMENTS FOR SUBCLUMPS

We measure the projected mass of subclump candidates (labeled in Figures 2 and 3) which are identified above the 3σ significant level in the mass map. The projected masses, $M_{\zeta_c}(<\theta)$, are estimated by the so-called ζ_c-statistics (Clowe et al. 2000) which is a modified version of the original one (Fahlman et al. 1994):

$$M_{\zeta_c}(<\theta) = \pi\theta^2 \Sigma_{\rm cr} \zeta_c(\theta, \theta_{\rm b1}, \theta_{\rm b2}), \quad (5)$$

where

$$\zeta_c(\theta, \theta_{\rm b1}, \theta_{\rm b2}) \equiv 2\int_\theta^{\theta_{\rm b1}} d\ln\theta \langle\gamma_+\rangle(\theta) + \frac{2}{1-\theta_{\rm b1}^2/\theta_{\rm b2}^2}\int_{\theta_{\rm b1}}^{\theta_{\rm b2}} d\ln\theta\langle\gamma_+\rangle(\theta) = \bar\kappa(<\theta) - \bar\kappa(\theta_{\rm b1} \leqslant \theta \leqslant \theta_{\rm b2}). \quad (6)$$

Here, θ is a given radius, and $\theta_{\rm b1}$ and $\theta_{\rm b2}$ are the inner and outer radii of the subtracted background region. The critical surface density $\Sigma_{\rm cr} = c^2/(4\pi G)(D_{\rm s}D_{\rm ls}/D_{\rm l})$ is given by the angular diameter distances to the cluster ($D_{\rm l}$), to the source ($D_{\rm s}$), and between the cluster and source ($D_{\rm ls}$). The M_{ζ_c} is a model-independent mass estimation.

We first obtain central positions of mass clumps by peak-finding algorithms and then redistribute them within $0\farcm2$ over 500 Monte Carlo simulations to take into account uncertainties of central positions. We choose the central position at which the S/N of the ζ_c measurement is at the maximum (Table 3). The background region is in the annulus of 40–100 kpc surrounding candidates so that we extract the substructure mass embedded in the cluster main potential. If the cluster potential is uniform within $\sim$100 kpc, it is a good mass estimate of subclumps. The following results are not changed by choosing the background region. As described in Equation (6), ζ_c mass measurement is computed by integrating the measured tangential shears outside a given radius θ. Since the available number for background galaxies in the outer annulus is larger than those in the inner one, it enables us to plot the M_{ζ_c} profile for each mass clump.

We also calculate LSS-corrected projected masses, $M_{\zeta_c}^{(\rm corr)}$, in terms of $\langle\gamma_+\rangle(\theta) - \langle\gamma_+^{(\rm LSS)}\rangle(\theta)$, where $\gamma_+^{(\rm LSS)}$ are the LSS shears obtained in Section 4.4. We do not consider the intrinsic shape noise. We note that $M_{\zeta_c}^{(\rm corr)}$ is the model-dependent mass because we assumed the mass-to-light ratio in a calculation of LSS shears, $\gamma_\alpha^{(\rm LSS)}$. Figure 8 shows the LSS-uncorrected and corrected projected mass profiles, respectively. The values of M_{ζ_c} are saturated on the outer radius, which indicates that the mass density of clumps is quite low on the outer radius. We estimate two-dimensional masses for each clump, $M_{\rm 2D}$ and $M_{\rm 2D}^{(\rm corr)}$, from the saturated values with a covariance matrix because each bin is correlated with each other. We list the resulting masses in Table 3. The LSS-uncorrected and corrected masses are in good agreement with each other, except for candidate 5. The LSS-corrected mass for candidate 5 is about half of that before the correction. Therefore, the background LSS effect significantly contributes to the lensing signals for candidate 5.

The mean values are $\langle M_{\rm 2D}^{(\rm corr)}\rangle = (4.8 \pm 1.41) \times 10^{12}\, h^{-1}\, M_\odot$ for all candidates and $\langle M_{\rm 2D}^{(\rm corr)}\rangle = (5.06 \pm 1.30) \times 10^{12}\, h^{-1}\, M_\odot$ except for candidate 5. They are at the order of the mass of cD galaxy halos, $M_{\rm 3D}^{(\rm SIS)}(\theta) = 3.0 \times 10^{12}\, h^{-1}\, M_\odot (\sigma_v/400\,{\rm km\,s^{-1}})^2 (r/40\,{\rm kpc})$, where σ_v is the velocity dispersion and we employ the velocity dispersion of the cD galaxy $\sim$200–400 km s^{-1} (e.g., Smith et al. 2000). Although we looked into the SDSS photometric and spectroscopic data, there is no correlation among the projected mass, and the velocity dispersion and luminosity of galaxies, which are located in each subclump.

6. TANGENTIAL SHEAR PROFILE STACKED OVER FIVE SUBCLUMPS

Since weak-lensing signals of the Coma Cluster at the low redshift are weak and the number of background galaxies within

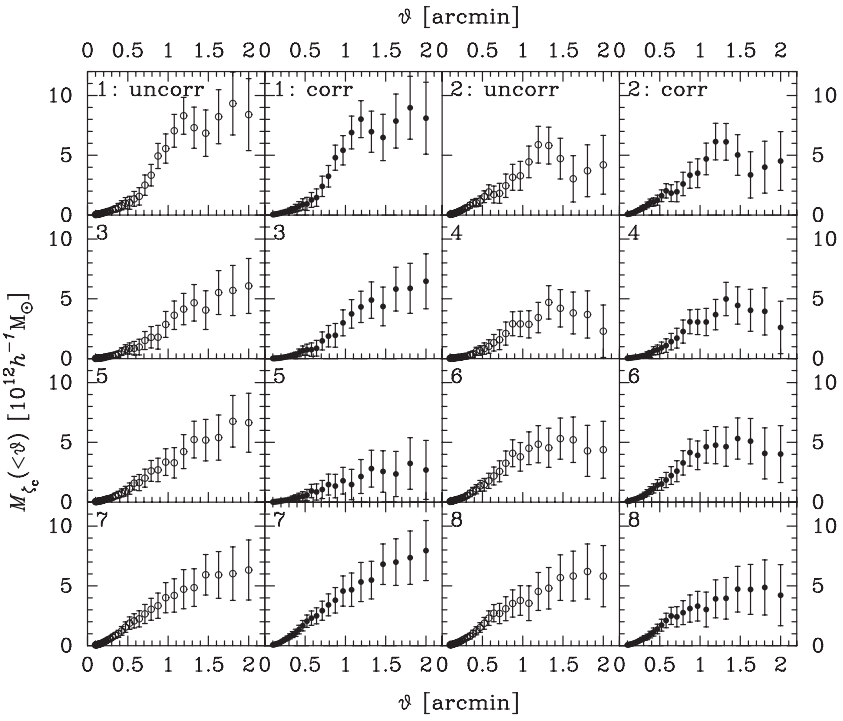

Figure 8. Aperture mass profile, M_{ζ_c}, for each subclump candidate (1–8). Open and filled circles represent aperture masses without and with an LSS correction, respectively. Aperture masses are saturated on the outer radii, which indicates that the mass density in the surroundings is quite low. It is consistent with the results of stacked lensing analysis (Section 6). The aperture mass for candidate 5, corrected by the LSS lensing effect, reduces to about half of that without an LSS correction.

a small radius is few, it is quite difficult to measure the tangential shear profile for each subclump candidate. We therefore measure a profile of tangential shear components by ensembling five subclump candidates. A mass measurement with a stacked tangential distortion profile is complementary to the ζ_c statistics (Section 5), because different shear catalogs are used in the two measurements. In the ζ_c statistics, source galaxies outside a given radius are used, while in the tangential shear measurement, source galaxies from the inner-to-outer radius are independently available. We here exclude two dark halos associated with cD galaxies in order to avoid a contamination of lensing distortion caused by the main cluster. Candidate 5, at which the projection effect is significant, is also ignored. The center for each subclump is chosen as the same position of the M_{ζ_c} measurements (Section 5). The averaged tangential shear distortions of source galaxies, $\langle g_+\rangle(\theta_n)$, are calculated in the circular annulus of the same radius, based on the same procedure as in Section 3. The typical projected distance between the center of a stacked tangential shear profile and the main cluster center, $\langle\theta_{\rm off}\rangle$, is obtained with a weight function of lensing signals, $\langle\theta_{\rm off}\rangle^2 = \sum_j \langle g_{+,j}\rangle^2\theta^2_{{\rm off},j}/\sum_j\langle g_{+,j}\rangle^2 \sim 17'.4$, where $\langle g_{+,j}\rangle$ is the lensing signal (Section 3) for each subclump and $\theta_{{\rm off},j}$ is an angular separation between each subclump and the main center.

We compute the LSS-corrected shear profile, $\langle g_+\rangle(\theta_n) - \langle g_+^{\rm (LSS)}\rangle(\theta_n)$, where the azimuthal average of the LSS distortion components, $\langle g_+^{\rm (LSS)}\rangle(\theta_n)$, is calculated without a statistical weight ($u_{g,i} = 1$). Figure 9 shows the stacked tangential shear profiles as a function of transverse separation θ with and without the LSS effect. We estimate the contribution of the main cluster mass on the stacked lensing signals, because the tangential shear provides full information on the lensing signals of gravitational potentials of both the main cluster and subclumps. It is necessary to calculate lensing distortions caused by the main cluster in order to measure the typical mass of the interior subhalos. We follow the convolution technique of Yang et al. (2006) to measure the azimuthally averaged convergence at the offset from the main cluster center in the lens plane. The values of g_+ of the offset main halo are at the order of $O(-10^{-5})$ in the range of the stacked lensing profile ($\theta < 6'$), which indicates that the lensing signals from the main cluster at the positions of subclumps are negligible.

Since the tidal field of the main cluster disrupts dark matter halos of the interior substructures, the subhalo radius would be determined by the tidal radius rather than the virial radius $r_{\rm vir}$. We therefore consider a truncated SIS model (TSIS) and a truncated NFW model (TNFW) for the tangential fitting, whose density profiles are truncated at the radius r_t:

$$\rho_{\rm TSIS}(r) = \frac{\sigma^2_{v,t}}{2\pi G r^2} \quad \text{for} \quad r \leqslant r_t \qquad (7)$$
$$= 0 \quad \text{for} \quad r > r_t$$

$$\rho_{\rm TNFW}(r) = \frac{M^{\rm (TNFW)}_{\rm sub}}{4\pi r^3_{s,t} m(c_t)} \frac{1}{(r/r_{s,t})(1+r/r_{s,t})^2} \quad \text{for} \quad r \leqslant r_t$$
$$= 0 \quad \text{for} \quad r > r_t, \qquad (8)$$

where $\sigma^2_{v,t}$ is the velocity dispersion for the TSIS model, $M^{\rm (TNFW)}_{\rm sub}$ and c_t are the mass and concentration for the TNFW model, and $r_{s,t} = r_t/c_t$ is the scale radius determined by the concentration and the truncated radius r_t. The subclump mass for the TSIS model is given by $M^{\rm (TSIS)}_{\rm sub} = 2\sigma^2_{v,t} r_t/G$.

Analytical expressions of the two-dimensional projection Σ of the density field are obtained by integration over $r_\parallel = [-\sqrt{r_t^2 - r^2}, +\sqrt{r_t^2 - r^2}]$:

$$\kappa_{\rm TSIS}(\theta) = \begin{cases} \frac{1}{\pi}\left(\frac{\theta_{E,t}}{\theta}\right)\arccos\left(\frac{\theta}{\theta_t}\right) & \text{for} \quad \theta \leqslant \theta_t \\ 0 & \text{for} \quad \theta > \theta_t, \end{cases}$$

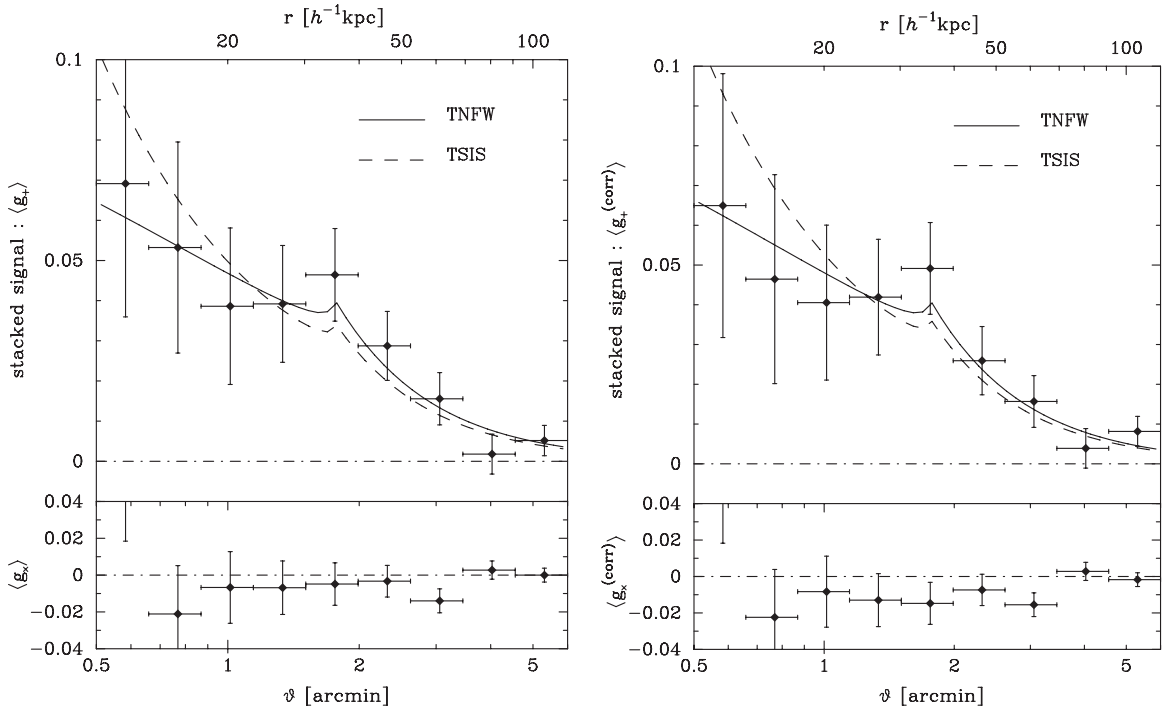

Figure 9. Profiles of the tangential shear component (top panel), g_+, and the 45° rotated component (bottom panel), $g_\times$, obtained from an ensemble of five subclumps. Left: the stacked profile from the original shear catalog. Right: the profile with an LSS lensing correction. The g_+ values clearly decrease over $\theta \sim 1\farcm75$. The solid and dashed lines are subhalo models of TSIS and TNFW, respectively.

where $\theta = r/D_l$ is an angular size of the three-dimensional radius and $\theta_{E,t} \equiv 4\pi(\sigma_{v,t}/c)^2 D_{\rm ls}/D_{\rm s}$ is the Einstein radius for the TSIS model:

$$\kappa_{\rm TNFW}(\theta) = \frac{M_{\rm sub}^{\rm (TNFW)}}{2\pi\Sigma_{\rm cr} r_{s,t}^2 m(c_t)} f(x), x = \theta/\theta_{s,t} \quad (9)$$

$$f(x) = \begin{cases} -\frac{\sqrt{c_t^2 - x^2}}{(1-x^2)(1+c_t)} + \frac{1}{(1-x^2)^{3/2}} \arccosh\left(\frac{x^2+c_t}{x(1+c_t)}\right) \\ \quad \text{for} \quad x < 1 \\ \frac{\sqrt{c_t^2-1}}{3(1+c_t)}\left(1+\frac{1}{1+c_t}\right) \\ \quad \text{for} \quad x = 1 \\ -\frac{\sqrt{c_t^2 - x^2}}{(1-x^2)(1+c_t)} - \frac{1}{(x^2-1)^{3/2}} \arccos\left(\frac{x^2+c_t}{x(1+c_t)}\right) \\ \quad \text{for} \quad 1 < x \leqslant c_t \\ 0 \quad \text{for} \quad c_t < x. \end{cases} \quad (10)$$

The expression of $f(x)$ is the same as that of Takada & Jain (2003) and Hamana et al. (2004), although for them, the mass density is truncated at the virial radius. We here do not assume $r_t = r_{\rm vir}$ because we aim to investigate disrupted interior substructures. The TSIS and TNFW profiles are specified in terms of two parameters, $\theta_{E,t}$ and θ_t, and three parameters, $M_{\rm sub}^{\rm (TNFW)}$, c_t, and θ_t, respectively.

We fit the LSS-uncorrected and corrected distortion profiles with the TSIS and TNFW models. The best-fit parameters are summarized in Table 4. Two models describe well the stacked tangential shear profile. The best-fit parameters with and without an LSS lensing correction do not change significantly. The truncated radii for the two models are in good agreements with each other. Indeed, the break in the tangential shear profile is clearly found at $\theta \sim 1\farcm75$ (Figure 9). The values of g_+ steeply decrease ($\propto \theta^{-2}$) over the truncated radius, which indicates that the halo mass density drops to zero at the truncated radius. It is consistent with the $\zeta_{\rm c}$ mass measurement (Section 5). This feature does not clearly appear in a stacked lens analysis for massive clusters of $M_{\rm vir} > 10^{14}\, h^{-1}\, M_\odot$ (Okabe et al. 2009). The TNFW and TSIS masses are in agreement with the mean projected mass $\langle M_{\rm 2D}^{\rm (corr)} \rangle_{34678} = (4.78 \pm 1.07) \times 10^{12}\, h^{-1}\, M_\odot$. We note that the two-dimensional mass for truncated mass models (TNFW and TSIS) has the same analytical expression as the three-dimensional mass ($M_{\rm 2D}^{\rm TSIS} = M_{\rm 3D}^{\rm TSIS}$ and $M_{\rm 2D}^{\rm TNFW} = M_{\rm 3D}^{\rm TNFW}$), because there is no projection effect due to the zero mass outside r_t.

We also investigate model fittings for spurious mass clumps appearing in mass maps simulated by the rotated shear catalog. First, we randomly rotate an angle in the (g_1, g_2) plane for each background galaxy with its $|g|$ fixed and then conduct the mass reconstruction for the background catalog by 500 times. Second, we detect peaks whose significance is over 3σ in mass maps. Third, we measure stacked tangential profiles for five peaks which are bootstrap re-sampled from detected peaks by 300 times. In the measurements, the peak whose distance from the cluster center is more than $10'$ is only used in order to avoid the main cluster lensing signal (Yang et al. 2006). The averaged χ^2's are $\langle \chi^2 \rangle = 9.9$ for the TNFW and $\langle \chi^2 \rangle = 15.7$ for TSIS models. Those χ^2's are worse than our results. This is why the form of the stacked tangential profile for spurious clumps is different from Figure 9.

7. DISCUSSION AND CONCLUSION

7.1. Cluster Mass Comparison

We compare our mass estimates with previous results of multi-wavelength data. The line-of-sight velocity distribution of member galaxies with the Jeans equation, which requires the assumption of the dynamical equilibrium, derived $M_{\rm vir} = 9.8 \times 10^{14} h^{-1}\, M_\odot$ and $c_{\rm vir} = 9.4$ for the NFW mass model (Łokas & Mamon 2003). Based on a caustic method to measure

Table 4
The Best-fit TSIS and TNFW Model Parameters

Model Parameter (1)	LSS Uncorrected (2)	LSS Corrected (3)
TSIS		
$M_{\rm sub}^{\rm (TSIS)}$ ($10^{12}\,h^{-1}\,M_\odot$)	$3.47^{+1.21}_{-0.56}$	$3.54^{+1.32}_{-0.54}$
θ_t (arcmin)	$1.76^{+0.57}_{-0.15}$	$1.76^{+0.61}_{-0.13}$
r_t (h^{-1} kpc)	$35.21^{+11.32}_{-2.98}$	$35.21^{+12.25}_{-2.58}$
$\sigma_{v,t}$ (km s^{-1})	$460.59^{+30.53}_{-32.70}$	$465.27^{+30.21}_{-32.31}$
χ^2/dof	4.4/7	5.3/7
TNFW		
$M_{\rm sub}^{\rm (TNFW)}$ ($10^{12}\,h^{-1}\,M_\odot$)	$3.90^{+1.22}_{-0.47}$	$4.00^{+1.45}_{-0.37}$
θ_t (arcmin)	$1.75^{+0.25}_{-0.26}$	$1.75^{+0.21}_{-0.29}$
r_t (h^{-1} kpc)	$35.01^{+4.99}_{-5.28}$	$35.01^{+4.21}_{-5.79}$
c_t	$1.53^{+1.12}_{-0.79}$	$1.53^{+0.74}_{-0.68}$
χ^2/dof	2.5/6	2.4/6

Notes. Column 1 (upper): name of best-fit parameters for the TSIS model (Equation (7)): the subhalo mass $M_{\rm sub}^{\rm (TSIS)}$, the truncated radius r_t, its angular radius θ_t, and the velocity dispersion $\sigma_{v,t}$. Columns 2 and 3 (upper): the best-fit parameters for the TSIS model without and with an LSS correction. Column 1 (lower): name of best-fit parameters for the TNFW model (Equation (8)): the subhalo mass $M_{\rm sub}^{\rm (TNFW)}$, the truncated radius r_t, its angular radius θ_t, and the concentration parameter c_t. Columns 2 and 3 (lower): the best-fit values for the TNFW model without and with an LSS correction. All parameters are determined by fitting the mean distortion profile which is obtained by staking the distortion signals for five clump candidates (3, 4, 6, 7, and 8). The χ^2/dof is the chi-square for best fits and the degree of freedom.

a characteristic pattern of line-of-sight velocities of galaxies falling into cluster potential (Kaiser 1987), Rines et al. (2003) obtained $M_{200} = 7.85 \times 10^{14} h^{-1}\,M_\odot$ and $c_{200} = 10$. Our result of NFW mass $M_{\rm vir}$ and M_{200} is in good agreement with their results, while our concentration parameter is lower. Our weak-lensing analysis is to use one-band imaging data. As demonstrated by Broadhurst et al. (2005; see also Umetsu & Broadhurst 2008; Okabe et al. 2009), the dilution contamination of member galaxies on lensing signals makes it problematic to obtain an accurate measurement of the concentration parameter. It is therefore important to correct the dilution effect by securely selecting of background galaxies in the color–magnitude plane (Broadhurst et al. 2005; Umetsu & Broadhurst 2008; Umetsu et al. 2009). In addition, we require the data to cover the virial radius in order to improve measurement accuracy of halo mass. The SDSS and CHFT weak-lensing results (Kubo et al. 2007; Gavazzi et al. 2009) are $M_{200} = 18.8^{+6.5}_{-5.6} \times 10^{14}\,M_\odot$ and $M_{200} = 5.1^{+4.3}_{-2.1} \times 10^{14}\,M_\odot$, and $c_{200} = 3.84^{+13.16}_{-0.18}$ and $c_{200} = 5.0^{+3.2}_{-2.5}$. They agree with our results within large errors. The *ASCA* and *ROSAT* X-ray observations with assumptions of hydrostatic equilibrium, and the isothermally and single β model show $M_{500} = 11.99^{+1.28}_{-1.29} \times 10^{14}\,M_\odot$ (Reiprich & Böhringer 2002) and $M_{500} = 9.95^{+2.10}_{-2.99} \times 10^{14}\,M_\odot$ (Chen et al. 2007), which are higher than our estimates. We cannot rule out a possibility that the low angular resolution of the *ASCA* satellite leads to a bias on mass estimates. It is of critical importance to compare the X-ray and weak-lensing masses of the Coma Cluster, which is the only cluster known to have turbulence in the intracluster medium (ICM). The *ASCA* and *XMM-Newton* X-ray observations (e.g., Watanabe et al. 1999; Arnaud et al. 2001) have shown the complex temperature variations in the ICM. Schuecker et al. (2004) have revealed a Kolmogorov/

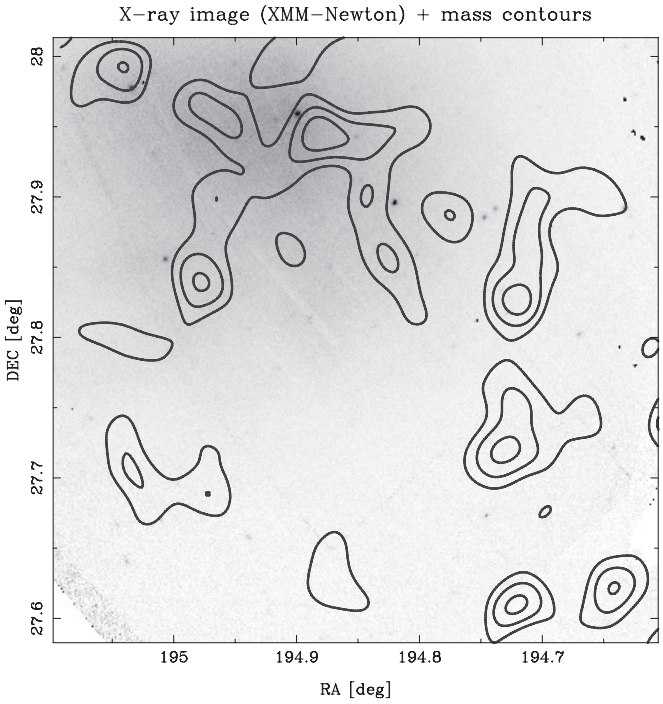

Figure 10. X-ray exposure-corrected image, no-subtracted backgrounds, overlaid with mass contours of the central $26' \times 26'$ cluster region.

Oboukhov-type turbulence spectrum in the ICM as a consequence of the projected pressure distributions. They constrained that the lower limit of turbulent pressure accounts for 10% of the total ICM pressure. Recent hydrodynamic *N*-body simulations pointed out that X-ray mass estimates with an assumption of hydrostatic equilibrium are biased low due to ICM turbulence, because the gas motion pressure of turbulence as well as bulk motions supports a part of the total pressure (e.g., Evrard et al. 1996; Nagai et al. 2007). Their results cast a doubt on accurate cluster mass measurement by X-ray analysis alone, which is a serious concern for cluster-based cosmological probes (e.g., Vikhlinin et al. 2009a, 2009b; Zhang et al. 2010). Therefore, a comparison of independent mass estimates is of great importance to understand, in a quantitative manner, how much the gas motion pressure affects the X-ray mass estimates (Kawaharada et al. 2010).

7.2. Comparison with X-ray Image

We compare an X-ray exposure-corrected image retrieved from archival data of *XMM-Newton* with mass counters of the central region (Figure 10). The *XMM-Newton* data in the outskirts region are lacking. The X-ray image shows some point sources associated with galaxies in clump candidates. The ICM distributions are not correlated with mass clump candidates. This is why the intracluster plasma can escape from the gravitational potential of subclumps. The sound velocity of the ICM is given by

$$c_s = \left(\frac{5k_BT}{3\,\mu m_p}\right)^{1/2} \simeq 1457 \left(\frac{k_BT}{8.25\,{\rm keV}}\right)^{1/2} {\rm km\,s^{-1}}, \quad (11)$$

where the temperature $k_BT = 8.25 \pm 0.10$ keV (Arnaud et al. 2001), the mean molecular weight $\mu = 0.62$, and m_p is the proton mass. The sound velocity is higher than the typical escape

velocity from subclumps, as below:

$$c_s \geqslant v_{\rm esc} = \left(\frac{2GM_{\rm sub}^{\rm (TNFW)}}{r_t}\right)^{1/2} \simeq 991\,{\rm km\,s^{-1}}. \quad (12)$$

Since the temperature of point sources is low, $k_BT \sim 1\,{\rm keV}$, with high metal abundance (Vikhlinin et al. 2001), its sound velocity is lower than the escape velocity.

7.3. Tidal Radius

The stacked tangential shear profile for five subclumps, excluding subhalos associated with cD galaxies and candidate 5, is well described by the TSIS and TNFW models. The fitting result gives the truncated radius $r_t \simeq 35\,h^{-1}\,{\rm kpc}$, which coincides with galaxy–galaxy lensing results in clusters (e.g., Natarajan & Springel 2004; Natarajan et al. 2007). The truncated radius is much smaller than a truncated radius ∼200 kpc obtained by galaxy–galaxy lensing studies of fields (e.g., Hoekstra et al. 2004). It would be due to the strong tidal field of the main cluster gravitational potential. The tidal radius of a subhalo orbiting in a spherically symmetric mass distribution of a cluster is obtained by the balance between the tidal force of the primary halo and the gravity of the subclump, $r_{\rm tidal} = (M_{\rm sub}/(M(<r_p)(2 - \partial \log M/\partial \log r_p))^{1/3} r_p$ (e.g., Tormen et al. 1998), where r_p is the pericenter radius, which is the minimal radius from the cluster center during its orbiting history. Since we do not constrain its pericenter radius directly from a current position and do not derive the three-dimensional radius, we instead assume the mean, projected offset radius $\langle\theta_{\rm off}\rangle$ of subclumps in stacked lensing analysis. Here, we assume the NFW and TNFW mass models for the main cluster and substructures, respectively. We obtain the tidal radius $r_{\rm tidal} \sim 42\,h^{-1}\,{\rm kpc}$, which coincides with the truncated radius $r_t \simeq 35\,h^{-1}\,{\rm kpc}$.

7.4. Subhalo Mass Fraction

We found four subhalos and two cD galaxy halos in the central data ($r \lesssim 30'$) and one halo in the outskirts data ($30' \lesssim r \lesssim 60'$). There is a difference of the halo number for the radius, which might support the results of numerical simulation (e.g., De Lucia et al. 2004; Gao et al. 2004) that the number of substructure increases as the radius decreases. Compensating the limitation of our data region, we roughly estimate the number of subhalos within the radii $r_{\rm vir}$ and r_{200}. If we assume that there are four ($r \lesssim 30'$) and one ($30' \lesssim r \lesssim 60'$) subhalos in the area corresponding to our data, the halo number is estimated to be $\pi(r_{\rm vir}^2 - 30\,{\rm arcmin}^2)/A_{\rm outskirts} + 4 \times (\pi\,30\,{\rm arcmin}^2/A_{\rm center}) + 2{\rm cDs}$, where A is the area of our data. The Poisson noise for distributions is applied for the statistical errors.

The halo number detected by weak-lensing analysis is expected to be $N_{\rm sub}(<r_{\rm vir}) = 43 \pm 30$ and $N_{\rm sub}(<r_{200}) = 27 \pm 15$. If the typical halo mass is the best-fit value $\langle M_{\rm sub}^{\rm (TNFW)}\rangle = 4.00 \times 10^{12}\,h^{-1}\,M_\odot$ obtained by fitting of the stacked tangential profile, the total substructure mass within the virial radius accounts for ∼19% ± 13% and 17% ± 9% of total cluster masses $M_{\rm vir}$ and M_{200}, respectively. Although the total mass fraction contained in subhalos does not agree with each other in the literature (e.g., De Lucia et al. 2004; Natarajan et al. 2007; Gao et al. 2004), most authors estimate it to be 5%–20%. Our result is in rough agreement with the numerical simulations. A galaxy–galaxy lensing study (Natarajan et al. 2007) indicates that 10%–20% of the mass is contained in cluster substructures, which also roughly agrees with our result.

Our weak-lensing analysis on the nearby cluster would indicate the possibility that the mass function of cluster substructures is measurable without assumptions of mass-to-light ratio for member galaxies and dynamical state, while the galaxy–galaxy lensing studies (e.g., Natarajan & Springel 2004; Natarajan et al. 2007) require the assumption of the mass and light scaling law. We however have not yet obtained the mass spectrum as the galaxy–galaxy lensing studies have done (e.g., Natarajan & Springel 2004; Natarajan et al. 2007).

An alternative possible approach to investigate the mass function of cluster substructures is to measure higher order moments of the lensed images (HOLICs) and using the moments to estimate the flexion (e.g., Okura et al. 2007, 2008; Okura & Futamase 2009). They have shown for the first time that flexion analysis can discover substructures using the image of A1689 (Okura et al. 2007).

As pointed out by Shaw et al. (2006), the median mass fraction is an increase function of the virial mass ($f_{\rm sub} \propto M_{\rm vir}^{0.44\pm0.06}$), because massive objects, which formed more recently than less massive objects, have less time to disrupt subhalos (Zentner et al. 2005). The statistical study of the mass fraction of galaxy clusters is, therefore, one of the good tests of ΛCDM and hierarchical clustering, as the concentration–mass relation of the NFW mass model (Okabe et al. 2009). Hence, further systematic study of mass fractions is required.

The area of our current data is insufficient to derive the halo mass function as well as to measure cluster mass accurately. The next instrument of a prime focus camera of the Subaru telescope, Hyper-Suprime-Cam, whose field of view is ∼1.5 deg^2, will efficiently observe the nearby cluster and enables us to conduct weak-lensing and flexion analyses. Our result using the Subaru/Suprime-Cam does guarantee that weak-lensing analysis using Subaru/Suprime-Cam and Hyper-Suprime-Cam is capable for almost X-ray clusters.

We gratefully thank the anonymous referee whose comments significantly improved the manuscript. We are grateful to N. Kaiser for developing the IMCAT package and making it publicly available. We thank R. Gavazzi for discussing CHFT weak-lensing analysis. N.O. gratefully thanks H. Hayashi, Y. Itoh, M. Chiba, M. Takada, K. Umetsu, and H. Nishioka for helpful discussions. N.O. and T.F. are supported in part by a Grant-in-Aid from the Ministry of Education, Culture, Sports, Science, and Technology of Japan (N.O.: 20740099; T.F.: 20540245) as well as the GCOE program "Weaving Science Web beyond Particle-matter Hierarchy" at Tohoku University and a Grant-in-Aid for Science Research in a Priority Area "Probing the Dark Energy through an Extremely Wide and Deep Survey with Subaru Telescope" (No. 18072001). Y.O. thanks the JSPS Research Fellowships for Young Scientists.

REFERENCES

Abazajian, K. N., et al. 2009, ApJS, 182, 543
Arnaud, M., et al. 2001, A&A, 365, L67
Broadhurst, T., et al. 2005, ApJ, 619, L143
Chen, Y., Reiprich, T. H., Böhringer, H., Ikebe, Y., & Zhang, Y.-Y. 2007, A&A, 466, 805
Clowe, D., Luppino, G. A., Kaiser, N., & Gioia, I. M. 2000, ApJ, 539, 540
Conselice, C. J., & Gallagher, J. S., III 1999, AJ, 117, 75
De Lucia, G., Kauffmann, G., Springel, V., White, S. D. M., Lanzoni, B., Stoehr, F., Tormen, G., & Yoshida, N. 2004, MNRAS, 348, 333
Duffy, A. R., Schaye, J., Kay., S. T., & Dalla, V. C. 2008, MNRAS, 390, L64
Erben, T., van Waerbeke, L., Bertin, E., Mellier, Y., & Schneider, P. 2001, A&A, 366, 717
Evrard, A. E., Metzler, C. A., & Navarro, J. F. 1996, ApJ, 469, 494

Fahlman, G., Kaiser, N., Squires, G., & Woods, D. 1994, ApJ, 437, 56
Gao, L., White, S. D. M., Jenkins, A., Stoehr, F., & Springel, V. 2004, MNRAS, 355, 819
Gavazzi, R., Adami, C., Durret, F., Cuillandre, J.-C., Ilbert, O., Mazure, A., Pelló, R., & Ulmer, M. P. 2009, A&A, 498, L33
Guzik, J., & Seljak, U. 2002, MNRAS, 335, 311
Hamana, T., Takada, M., & Yoshida, N. 2004, MNRAS, 350, 893
Hoekstra, H., Hsieh, B. C., Yee, H. K. C., Lin, H., & Gladders, M. D. 2005, ApJ, 635, 73
Hoekstra, H., Yee, H. K. C., & Gladders, M. D. 2004, ApJ, 606, 67
Johnston, D. E., et al. 2007, arXiv:0709.1159
Kaiser, N. 1987, MNRAS, 227, 1
Kaiser, N., & Squires, G. 1993, ApJ, 404, 441
Kaiser, N., Squires, G., & Broadhurst, T. 1995, ApJ, 449, 460
Kawaharada, M., et al. 2010, ApJ, in press (arXiv:1002.4811)
Kubo, J. M., Stebbins, A., Annis, J., Dell'Antonio, I. P., Lin, H., Khiabanian, H., & Frieman, J. A. 2007, ApJ, 671, 1466
Łokas, E. L., & Mamon, G. A. 2003, MNRAS, 343, 401
Mandelbaum, R., Tasitsiomi, A., Seljak, U., Kravtsov, A. V., & Wechsler, R. H. 2005, MNRAS, 362, 1451
Miyazaki, S., et al. 2002, PASJ, 54, 833
Miyazaki, S., et al. 2007, ApJ, 669, 714
Nagai, D., Vikhlinin, A., & Kravtsov, A. V. 2007, ApJ, 655, 98
Nakamura, T. T., & Suto, Y. 1997, Prog. Theor. Phys., 97, 49
Natarajan, P., De Lucia, G., & Springel, V. 2007, MNRAS, 376, 180
Natarajan, P., & Springel, V. 2004, ApJ, 617, L13
Navarro, J. F., Frenk, C. S., & White, S. D. M. 1996, ApJ, 462, 563
Okabe, N., Takada, M., Umetsu, K., Futamase, T., & Smith, G. P. 2009, PASJ, submitted (arXiv:0903.1103)
Okabe, N., & Umetsu, K. 2008, PASJ, 60, 345
Okura, Y., & Futamase, T. 2009, ApJ, 699, 143
Okura, Y., Umetsu, K., & Futamase, T. 2007, ApJ, 660, 995
Okura, Y., Umetsu, K., & Futamase, T. 2008, ApJ, 680, 10
Ouchi, M., et al. 2004, ApJ, 611, 660
Oyaizu, H., Lima, M., Cunha, C. E., Lin, H., Frieman, J., & Sheldon, E. S. 2008, ApJ, 674, 768
Reiprich, T. H., & Böhringer, H. 2002, ApJ, 567, 716
Rines, K., Geller, M. J., Kurtz, M. J., & Diaferio, A. 2003, AJ, 126, 2152
Schuecker, P., Finoguenov, A., Miniati, F., Böhringer, H., & Briel, U. G. 2004, A&A, 426, 387
Seljak, U. 2000, MNRAS, 318, 203
Shaw, L. D., Weller, J., Ostriker, J. P., & Bode, P. 2006, ApJ, 646, 815
Smith, R. J., Lucey, J. R., Hudson, M. J., Schlegel, D. J., & Davies, R. L. 2000, MNRAS, 313, 469
Takada, M., & Jain, B. 2003, MNRAS, 340, 580
Tormen, G., Diaferio, A., & Syer, D. 1998, MNRAS, 299, 728
Umetsu, K., & Broadhurst, T. 2008, ApJ, 684, 177
Umetsu, K., et al. 2009, arXiv:0908.0069
Vikhlinin, A., Markevitch, M., Forman, W., & Jones, C. 2001, ApJ, 555, L87
Vikhlinin, A., et al. 2009a, ApJ, 692, 1033
Vikhlinin, A., et al. 2009b, ApJ, 692, 1060
Watanabe, M., Yamashita, K., Furuzawa, A., Kunieda, H., Tawara, Y., & Honda, H. 1999, ApJ, 527, 80
Yagi, M., Kashikawa, N., Sekiguchi, M., Doi, M., Yasuda, N., Shimasaku, K., & Okamura, S. 2002, AJ, 123, 66
Yang, X., Mo, H. J., van den Bosch, F. C., Jing, Y. P., Weinmann, S. M., & Meneghetti, M. 2006, MNRAS, 373, 1159
Yoshida, M., et al. 2008, ApJ, 688, 918
Zentner, A. R., Berlind, A. A., Bullock, J. S., Kravtsov, A. V., & Wechsler, R. H. 2005, ApJ, 624, 505
Zhang, Y.-Y., et al. 2010, ApJ, 711, 1033